Hindawi
Journal of Chemistry
Volume 2022, Article ID 2705848, 8 pages
https://doi.org/10.1155/2022/2705848

Research Article

Luminescence and Preventive Effect of Two New Cd(II) Compounds on Scar Formation after Cosmetic Surgery

Zhi-Ming Yuan, Ze-Xu Lin, Shui-Lian Chen, and Xin Lin

Plastic Cosmetic Surgery, Quanzhou First Hospital Affiliated to Fujian Medical University, Quanzhou, Fujian, China

Correspondence should be addressed to Zhi-Ming Yuan; zhanli55878@stu.ahu.edu.cn

Received 24 May 2022; Revised 18 July 2022; Accepted 27 July 2022; Published 24 August 2022

Academic Editor: Radhey Srivastava

Two coordination polymers involving Cd(II), i.e., $[Cd_2(IDPA)_2(bpe)\ (H_2O)_2]_n{\cdot}2n(H_2O)$ (1) (H_2IDPA is 5-(1-oxoisoindolin-2-yl) isophthalic acid, bpe is 1,2-bis(4-pyridyl)ethane, 4-bpmh is N, N-bis-pyridin-4-ylmethylene-hydrazine), and $[Cd(IDPA)(4\text{-}bpmh)_{0.5}(H_2O)_2]_n{\cdot}n(H_2O)$ (2) are prepared under solvothermal conditions *via* tuning the auxiliary ligand from bpe to 4-bpmh. Moreover, the as-prepared complexes 1–2 reveal much stronger luminescence in contrast to that of the free organic ligands. Their preventive effect and mechanism on scar formation after cosmetic surgery was explored. First, the two complexes' suppression of the viability of the human immortal keratinocyte line (HaCaT) cell line was examined via exploiting cell counting kit-8 (CCK-8) detection. The vascular endothelial growth factor (VEGF) signal pathway activation in HaCaT cells was detected by real-time reverse transcription-polymerase chain reaction (RT-PCR) assay.

1. Introduction

The healing of postoperative incisions is a complicated pathophysiological process, and multiple factors such as gene expression regulation and secretion regulation of various growth factors will affect the incision healing and cause scar formation [1]. To prevent and treat postoperative scar formation, it is necessary not only to understand the skin anatomy and incision healing mechanism but also to select the appropriate suture materials to minimize postoperative scar formation through professional wound suture techniques and appropriate physical and chemical intervention methods [2, 3]. There are many physical and chemical intervention methods for the prevention and treatment of postoperative scar formation, but the mechanism is not very clear [4]. It is of great significance to conduct in-depth study of postoperative scar prevention and treatment.

In the past few decades, the research on metal-organic frameworks (MOFs) has aroused widespread attention on account of the fascinating topological skeletons of MOFs, simultaneously due to their underlying applications as functional materials in various areas of magnetism, luminescence, catalysis, H_2 storage ect [5–8]. These promising application properties of MOFs constantly inspire us to design and construct new functional MOFs. Although achieving controlled syntheses of MOFs containing desired architectures and performances is still one of the biggest challenges for us, some effective methods for the syntheses of MOFs, the like mixed-ligand approach, pillar-layer method, post-synthetic modification as well as second building subunit method, have been successfully developed after lots of hard works by chemists [9–12], and numerous reports have demonstrated the effectiveness of these synthetic strategies for the construction of MOFs with predictable structures [13–15]. Given the importance of luminescent MOFs for the detection of pollutants, considerable efforts have been devoted to the construction of luminescent MOFs [16–18]. According to the reports, one good choice to prepare the luminescent MOFs is using a large π-conjugated organic ligand with multicoordination sites, and the large π-conjugated fluorophore of the organic ligand is helpful to enhance the luminescence of MOFs [19, 20]. H_2IDPA containing large π-conjugated fluorophore has been widely used by Ye and his co-workers to construct lots of MOFs

with intense luminescence at room temperature [21, 22]. In view its good coordination affinity and capability to d^{10} metal ions, in this work, we selected it in combination with N-donor ligands utilized as organic building backbones for assembling with the Cd(II) ions under the conditions of solvothermal. Through altering auxiliary ligands, we created two fresh compounds involving Cd(II), i.e., $[Cd_2(IDPA)_2(bpe)(H_2O)_2]_n{\cdot}2n(H_2O)$ (1) and $[Cd(IDPA)(4\text{-bpmh})_{0.5}(H_2O)_2]_n{\cdot}n(H_2O)$ (2). In addition, we also systematically investigated the fluorescent performances together with the thermal stabilities of the above compounds. Furthermore, the preventive effect and mechanism of the compound on scar formation after cosmetic surgery was determined.

2. Experimental Methods

2.1. Materials and Instrumentation. $Cd(NO_3)_2{\cdot}4H_2O$ (99.9%, Ar) was purchased from Sigma-Aldrich reagent company (Beijing, China), all the organic ligands used in this study were provided by Jinan Henghua Technology Co., Ltd; the solvent DMF was supplied by Tianjin Kangkede Chemical reagent company, the pure water used in this study was obtained from Hangzhou Wahaha Group Co. Ltd. (Hangzhou, China). The pH of the pure water was 6.83 ± 0.05, and its electrical conductivity was $1.82 \pm 0.20\ \mu$S/cm. For exploring the elements of N, C together with H, the Vario EL III analyzer was exploited. Varian 800 The PANalytical X/Pert Pro was utilized to investigate PXRD at 0.05° step size with 1.54056 Å·Cu/Kα radiation. The thermogravimetric analyses for as-generated CPs were implemented via the term analyzer of NETSCHZ STA-449C with an increasing rate of 10°C/min under the nitrogen flow at a temperature between 30 and 800. The Edinburg FLS920 TCSPC could be implemented for analyzing luminescent performances of the complexes at RT.

Synthesis of $[Cd_2(IDPA)_2(bpe)(H_2O)_2]_n{\cdot}2n(H_2O)$ (1) and $[Cd(IDPA)(4\text{-bpmh})_{0.5}(H_2O)_2]_n{\cdot}n(H_2O)$ (2).

The mixture formed by 0.1 mmol of $Cd(NO_3)_2{\cdot}4H_2O$, 0.1 mmol H_2L, 0.1 mmol bpe, 1 mL DMF, and 2 mL H_2O was placed into a small glass vial (20 mL) and heated under a temperature of 110°C for three days. After cooling the above mixture to RT gradually, the colorless massive crystals of compound 1 were gathered with a yield of 48 percent by $Cd(NO_3)_2{\cdot}4H_2O$. Anal. Calcd. (%) for $C_{44}H_{36}N_4O_{14}Cd_2$: N, 5.24, C, 49.37 and H, 3.37. Found (%): N, 5.21, C, 49.34 and H, 3.41. IR (KBr pellet) (υ/cm^{-1}): 3382 (s), 2926 (m), 2362 (m), 1942 (w), 1826 (w), 1609 (s), 1547 (s), 1400 (s), 1312 (s), 1186 (m), 1111 (m), 1053 (w), 1012 (m), 901 (w), 859 (m), 778 (m), 745 (m), 705 (w), 674 (w), 587 (w), 487 (m).

The mixture synthesized via 0.1 mmol of $Cd(NO_3)_2{\cdot}4H_2O$, 0.2 mmol of 4-bpmh, 0.1 mmol H_2L, 1 mL DMF, and 2 mL H_2O was placed into a small glass vial (20 mL) and heated under a temperature of 110°C for three days. After cooling the above mixture to RT gradually, the colorless massive crystals of compound 2 were gathered with the yield of 38 percent in the light of $Cd(NO_3)_2{\cdot}4H_2O$. Anal. Calcd. (%) for $C_{22}H_{21}N_3O_8Cd$: N, 7.40, C, 46.49, and H, 3.70. Found (%): N, 7.38, C, 46.52 and H, 3.72. IR (KBr pellet) (υ/cm^{-1}): 3385 (m), 2360 (w), 1944 (w), 1829 (w), 1610 (m), 1583 (m), 1534 (m), 1446 (m), 1398 (w), 1315 (w), 1186 (w), 1142 (w), 1109 (w), 1051 (w), 1014 (w), 922 (w), 905 (w), 862 (w), 810 (w), 779 (m), 746 (w), 709 (w), 670 (w), 635 (w), 592 (w), 526 (w), 477 (w), 426 (w).

2.2. X-Ray Crystallography. For the above complexes, their crystal architectures were measured by Mercury CCD that was controlled through the computer via exploiting 0.71073 Å graphite mono-chromated Mo–Kα radiation at RT. Moreover, the complexes' architectures could be solved via applying direct approaches by *ShelXS* and subsequently optimized through full-matrix least-squares strategies through the software of *SHELXL*-2014 according to F^2 [23]. The compounds' crystallographic data along with architectural optimizations are exhibited in Table 1. Table S1 reflects the chosen bond angles (o) together with the lengths (Å) of as-created complexes. Table S2 exhibits the specific H-bond parameters for them.

2.3. CCK-8 Determination. The CCK-8 detection was performed for examining the complexes' biological activity, and their inhibitory effect against the HaCaT cell's viability was tested. This study was finished following the instructions along with a slight change. Shortly, the HaCaT cells in the phage of logical growth were gathered and inoculated into plates (96 well). The cells were cultivated in 37°C incubators with 5% CO_2 humidified surrounding for half a day, the compound was subsequently added into wells for the treatment at 1, 2, 4, 8, 10, 20, 40, 80 μM concentration for two days. After that, CCK-8 reagents (10 μl) were utilized to incubate the cells for four hours, and the values of absorbance (optical density, OD) of each well were tested through a microplate spectrophotometer system (Molecular Devices, Sunnyvale, CA, USA) at 450 nm. This study was carried out in triplicate, and the results were described with mean ± standard deviation.

2.4. Real Time RT-PCR. The real-time RT-PCR was accomplished for the measurement of the complexes' reduction effect against the VEGF signal pathway activation in HaCaT cells. The experiment was carried out fully based on the protocols after some changes. Briefly, the HaCaT cells in the stage of logical growth were gathered and then inoculated into plates (96 well). The cells were cultivated in 37°C incubators with a 5% CO_2 humidified surrounding for twelve hours, next, the wells were added with a compound for performing the treatment. Subsequently, the cells were gathered and the extraction of overall RNA in tissue was conducted through TRIZOL reagent. After testing its quality and quantity, it was next reverse transcript into cDNA. Eventually, the real-time RT-PCR was carried out for determining the VEGF signal pathway relative expression in HaCaT cells, using the GAPDH as an internal control.

3. Results and Discussion

3.1. Crystal Structure of Compound 1. X-ray crystallographic investigations exhibited that 1 belongs to the monoclinic space group of *P*n, revealing a 2-dimensional extended

Table 1: The compounds' crystallographic data along with architectural optimizations.

Sample	1	2
Formula	$C_{44}H_{36}N_4O_{14}Cd_2$	$C_{22}H_{21}N_3O_8Cd$
*F*w	1069.57	567.84
Crystal system	Monoclinic	Monoclinic
Space group	*P*n	$P2_1/c$
a (Å)	14.0662 (12)	10.6556 (6)
b (Å)	10.1504 (4)	17.4949 (10)
c (Å)	15.6798 (12)	11.4139 (8)
α (°)	90	90
β (°)	113.993 (4)	96.883 (6)
γ (°)	90	90
Volume (Å^3)	2045.3 (3)	2112.4 (2)
Z	2	4
Density (calculated)	1.737	1.782
Abs. Coeff. (mm^{-1})	1.117	1.091
Total reflections	15136	10380
Unique reflections	8692	4459
Goodness of fit on F^2	1.026	1.199
Final *R* indices [$I > 2$sigma (I^2)]	R [a] = 0.0203, wR_2 [b] = 0.0492	R = 0.0803, wR_2 = 0.2393
R (all data)	R = 0.0211, wR_2 = 0.0496	R = 0.0866, wR_2 = 0.2440

[a] $R_1 = \Sigma||F_o|-|F_c||/\Sigma|F_o|$. [b] $wR_2 = |\Sigma w(|F_o|^2-|F_c|^2)|/\Sigma|w(F_o)^2|^{1/2}$, where $w = 1/[2(F_o^2) + (aP)^2 + bP]$. $P = (F_o^2 + 2F_c^2)/3$.

layered architecture. Each fundamental unit of compound 1 includes two isolated Cd(II) ions, two $IDPA^{2-}$, a bpe, two free, and two coordinated molecules of H_2O. Based on Figure 1(a), Cd1 ion, and Cd2 ion are 7-coordinated and exhibit slightly twisted pentagonal bipyramidal structures, they are defined through 5 carboxylic acid oxygen atoms offered by three $IDPA^{2-}$, a pyridyl N atoms belong to a bpe ligand and a terminal H_2O ligand. The bond separations of Cd–O/N varying from 2.242 (3) to 2.572 (3) Å are all by the reported compounds based on Cd(II) [24]. The $IDPA^{2-}$ in complex 1 utilities as a μ_3-bridge with its two carboxylic acid groups in diverse coordination manners: bridging-chelating together with chelating modes (Figure S1(a)). Two consecutive Cd(II) ions are bridged through 2 carboxylic acid groups provided by $IDPA^{2-}$ into a dinuclear subunit of $[Cd_2(COO)_2]$ with Cd$\cdots$Cd separation of 3.78 Å, and thus, the above subunits are deeply bridged via $IDPA^{2-}$ ligands to produce a 1-dimensional chain motif extending along the crystallographic direction *b* (Figure 1(b)). Through the coordination of bpe to the Cd(II) ions, these 1D chains are connected , generating a 2D layer structure (Figure 2(c)). By considering the dinuclear subunits and organic ligands as 4-connected nodes and linear connectors, for example, 2-dimensional layer can be reduced into a 4-bridged SQL tetragonal plane net (Figure S2(a)). Notably, the H atoms of the coordinated H_2O molecules can be accepted suitably by the carboxylic acid oxygen atoms belonging to another neighboring 2-dimensional layer, creating weak intermolecular H-bonding interactions that are revealed in Table S2. Hence, these weak H-bonding interactions deeply glued these 2-dimensional layers into a 3-dimensional supramolecular skeleton (Figure 2(d))

3.2. Crystal Structure of Compound 2. When bpe was substituted via another longer bis(pyridyl)-based ligand of 4-bpmh, compound 2 was successfully obtained that also crystallizing the monoclinic space group of $P2_1/c$. And its structured unit contains a Cd(II) ion, an $IDPA^{2-}$, 0.5 4-bpmh ligands, and a free and two coordinated molecules of H_2O. According to Figure 2(a), Cd1 is 7-coordinated via 4 carboxylic acid oxygen atoms belonging to two $IDPA^{2-}$, two coordinated H_2O molecules, a pyridyl N atom coming from a 4-bpmh, and the Cd1 ion coordination structure can be expressed as slightly twisted pentagonal bipyramid. The Cd–O/N separations vary from 2.299 (6) to 2.556 (6) Å, which are comparable with the lengths of reported compounds based on Cd(II) [20]. The $IDPA^{2-}$ in compound 2 employs a μ_2-bridge with the two carboxylic acid groups of $IDPA^{2-}$ ligand in the uniform chelating manner (Figure S1(b)). The Cd(II) ions are bridged μ_2-bridges of $IDPA^{2-}$ ligands, providing a 1-dimensional zigzag chain architecture along crystallographic axis *b* (Figure 1(b)), and in the above chain, the length of Cd$\cdots$Cd isolated through $IDPA^{2-}$ is 9.68 Å. These neighboring 1-dimensional chains are associated together by the coordination of the 4-bpmh ligands, creating a 2-dimensional layer along plane *bc* (Figure 2(c)). By regarding the organic ligands and Cd(II) ions as 3-bridged nodes and linear connectors, this 2D layer of 2 represents a 3-connected hcb net (Figure S2(b)). Although both compounds 1 and 2 show 2D layered structures, the different coordination patterns of $IDPA^{2-}$ ligand result in their different structural features and topological nets. In 2, H-bonding interactions are also present between the carboxylic acid oxygen atoms coming from one layer and the coordination H_2O molecules of another layer, and the specific H-bond parameters are reflected in Table S1. Therefore, the 3-connected hcb-type 2D layers are finally associated together via the intermolecular H-bonds, producing a 3-dimensional supramolecular skeleton (Figure 2(d)).

3.3. Powder X-Ray Diffraction (PXRD) Patterns and Thermogravimetric Analyses (TGA). The PXRD analyses outcomes on polycrystalline samples of 1–2 are shown in Figure

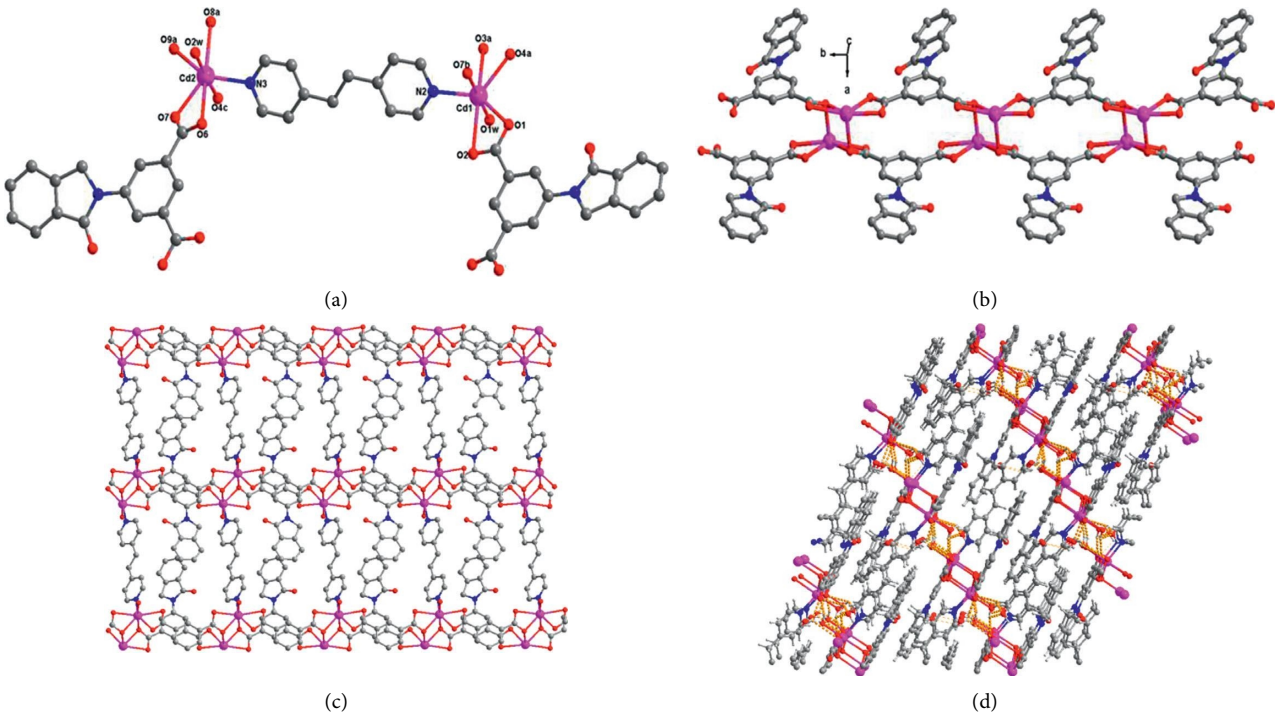

Figure 1: (a) The 1's coordination surroundings of Cd(II) ions. (b) The 1-dimensional chain architecture was established via the dinuclear subunits [Cd2(COO)2] and $IDPA^{2-}$. (c) The 2-dimensional layered structure of compound 1. (d) The 3D supramolecular structure of compound 1 is linked through intermolecular H-bonds.

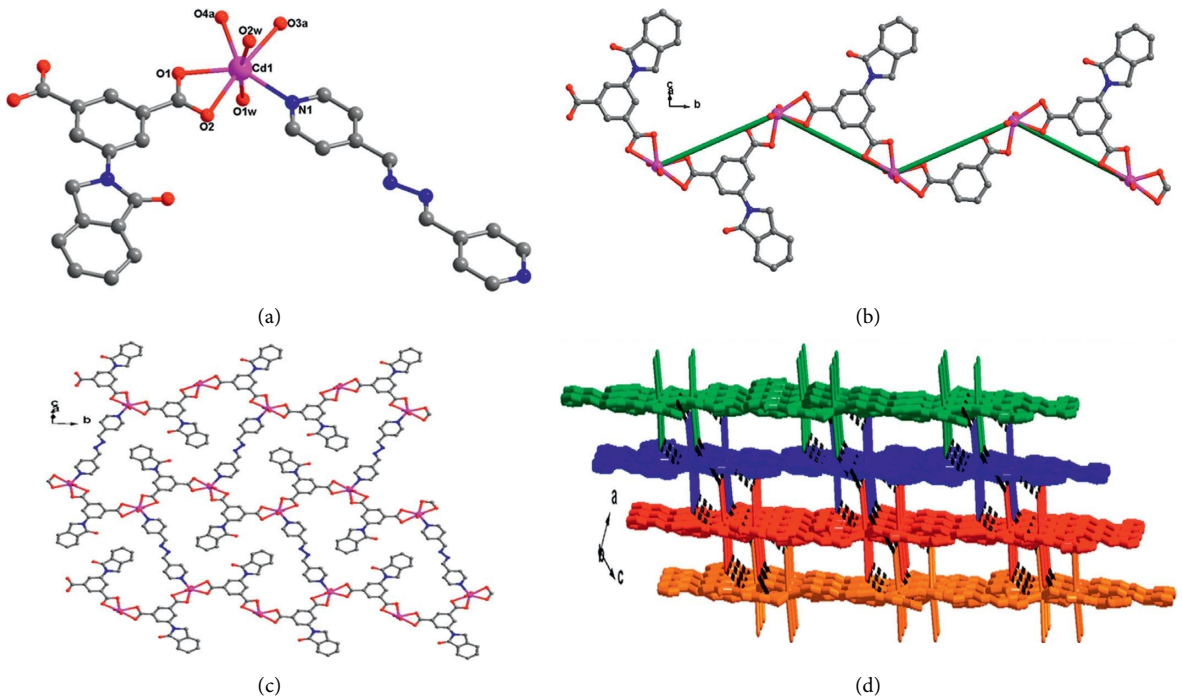

Figure 2: (a) The 2's coordination surroundings of Cd(II) ions. (b) The 1-dimensional zigzag chain architecture in complex 2. (c) The 2's 2-dimensional layered structure. (d) The 2's 3D supramolecular structure the linked *via* intermolecular H-bonds.

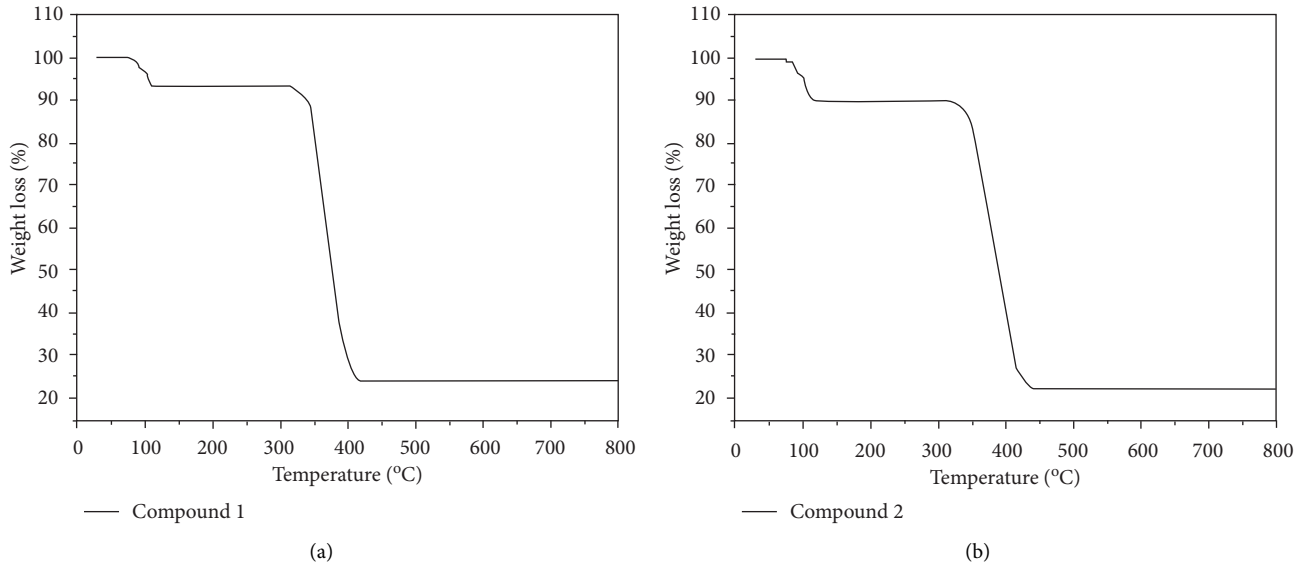

Figure 3: The curves of TGA (a) for the compounds 1 and (b) 2.

S3, from which we can see that there is great accordance of peak positions between the experimental and simulated patterns, indicating excellent homogeneity and purity of as-prepared bulk samples.

Moreover, we also explored the compounds' thermal behaviors under nitrogen flow between 30 and 800°C, and the study outcomes are revealed in Figure 3. In the compound 1's curve of TGA, 6.70% of weight loss existed at a temperature of 75–110°C and this is on account of the loss of the free together with the coordinated molecules of water (with 6.74% calculated value), and then when the temperature reaches 312°C, the 1's weight can be stable, and thereafter, significant weight loss occurred from 312 to 418°C, which is associated with the organic ligand decomposition. For compound 2, the loss of the lattice and coordinated H_2O molecules appeared from 75–122°C with an observed weight loss of 9.56% (calcd: 9.51%), and the collapse of the framework occurred in the range of 307–441°C because of the organic ligand decomposition.

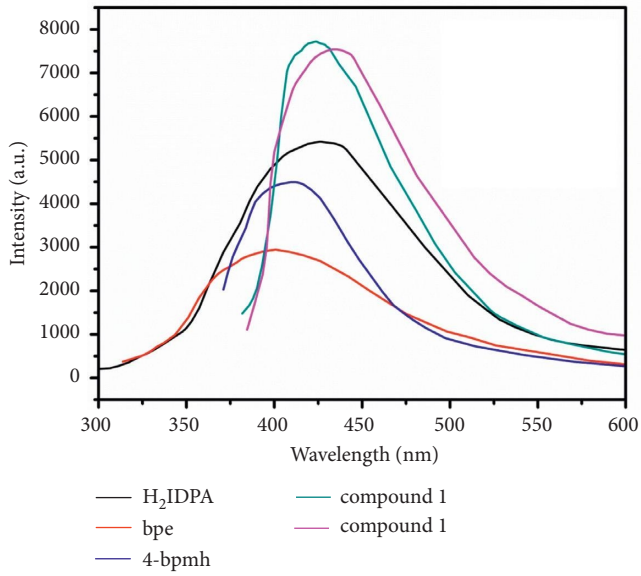

Figure 4: The luminescent emission spectra of the associated free organic ligand and the complexes at RT. Compound significantly reduces the viability of the HaCaT cells.

3.4. Photoluminescent Properties of 1–2. The transition metal compounds based on d^{10} generally exhibited outstanding luminescent performances for the potential application of luminescence sensing [25, 26]. Hence, in this work, the compounds' luminescent spectra were detected at RT, and with the aim of further under the luminescence nature, the luminescent spectra of associated free ligands were also gathered under identical conditions. Based on Figure 4, the 4-bpmh, bpe, and H_2IDPA emission spectra have maximum emission peaks at about 411 nm ($\lambda_{ex} = 330$ nm), 400 nm ($\lambda_{ex} = 320$ nm), 426 nm ($\lambda_{ex} = 345$ nm), respectively, and these emissions may be caused by π^* to n or π orbital transitions [23]. The compounds' emission spectra reveal the emission bands centered at 423 nm ($\lambda_{ex} = 340$ nm) and 434 nm ($\lambda_{ex} = 340$ nm). In comparison with N-donor ligands, the compounds' emission spectra show obvious redshifts, and compared to the carboxylate ligand of H_2IDPA, complex 1's emission spectrum has a 3 nm blue-shift and compound 2's emission spectrum has an 8 nm red-shift. Taking into consideration of the d^{10} configuration for Cd(II) and Zn(II) ions, the compounds' luminescence emissions may be on account of ligand-to-ligand charge transfer or intraligand emission or the mixture of ligand-to-ligand charge transfer and intraligand emission [15]. In contrast to free ligands, much stronger luminescence emissions of the complexes principally resulted from the coordination of ligand to the metal ions that can significantly upregulate the rigidity of the organic ligand.

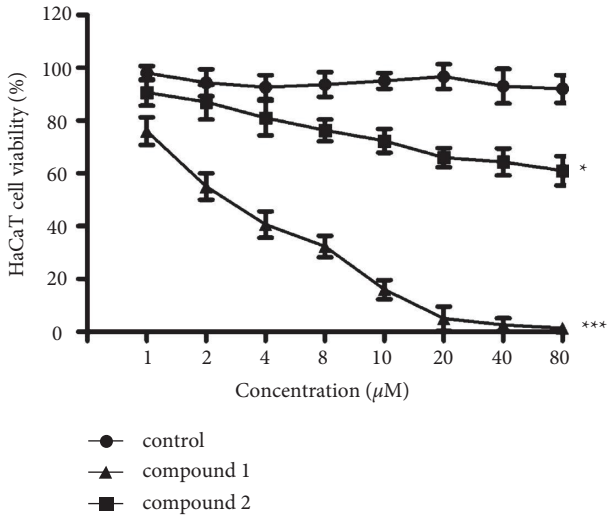

Figure 5: Markedly downregulate the viability of the HaCaT cells after treatment of as-created compound. The complexes were employed for treating HaCaT cell with various dilutions. The HaCaT cells viability was measured through CCK-8 detection. *means $P < 0.05$ and *** means $P < 0.005$. Compound inhibited the activation of the VEGF signal pathway in the HaCaT cells.

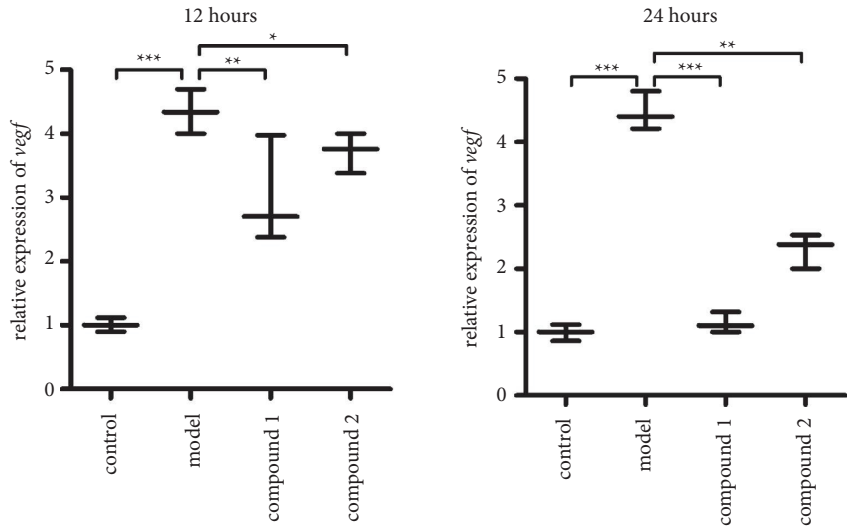

Figure 6: Evidently suppressed VEGF signal pathway activation in HaCaT cells after treating via the compound. The complexes were employed for treating HaCaT cells with specific concentrations. The real-time RT-PCR was conducted and the VEGF signal pathway activation in HaCaT cells was examined. *means $P < 0.05$, ** means $P < 0.01$, and ***means $P < 0.005$.

After creating compounds, their inhibitory activity against the viability of the HaCaT cells was tested. Hence, the CCK-8 detection was implemented in this paper. Based on Figure 5, it can be found that the 1 could markedly downregulate the HaCaT cell's viability. Nonetheless, 2 only exhibited a little effect on the HaCaT cell's viability. This result suggested the complex 1 treatment activity was much stronger in contrast to 2.

As previously described, complex 1 revealed superb inhibitory activity on the HaCaT cells viability. As the important role of the VEGF signal pathway in the viability of the HaCaT cells , the real time RT-PCR was deeply performed to test the VEGF signal pathway activation in the HaCaT cell. The results in Figure 6 exhibit that HaCaT cells have higher VEGF signal pathway activation level than control group. After treating via the compound 1, the activation of VEGF signal pathway in HaCaT cells was markedly downregulated, which is much superior to 2.

4. Conclusions

In the current paper, we prepared two compounds based on Cd(II) that were prepared under solvothermal conditions. The structural variations of 1–2 were achieved *via* regulating the N-donor auxiliary ligands: 4-connected SQL-type 2D net for 1 and 3-connected hcb-type 2D net for 2. Finally, these

2D layers are glued together *via* the intermolecular hydrogen bonds, affording 3D supramolecular frameworks. The compounds' strong luminescence emissions reveal that $IDPA^{2-}$ is an outstanding organic building backbone for building luminescent hybrid materials. The outcomes of CCK-8 detection suggested that 1 was superior to complex 2 in decreasing the viability of the HaCaT cells. The VEGF signal pathway activation in HaCaT cells was also suppressed via complex 1, instead of 2. Eventually, with the previous experiments, compound 1 was more outstanding than 2 in treating scar formation after cosmetic surgery.

Conflicts of Interest

The authors declare that they have no conflicts of interest.

Acknowledgments

The research was supported by Quanzhou Municipal Science & Technology Project (2020C036R) and Natural Science Foundation of Fujian Province (2019J01595).

Supplementary Materials

Selected bond lengths (Å) and angles (°) for compounds 1-2 (Table S1); The detailed hydrogen bond parameters for 1-2 (Table S2); The coordination modes of IDAP2- ligand (a) for 1 and (b) for 2 (Figure S1); (a) The 4-connected SQL net for 1. (b) The 3-connected hcb net for 2 (Figure S2); The PXRD patterns (a) for compound 1 and (b) for compound 2 (Figure S3), the information could be found in the supporting information file. (*Supplementary Materials*)

References

[1] G. Grabowski, M. J. Pacana, and E. Chen, "Keloid and hypertrophic scar formation, prevention, and management: standard review of abnormal scarring in orthopaedic surgery," *Journal of the American Academy of Orthopaedic Surgeons*, vol. 28, no. 10, pp. e408–e414, 2020.

[2] T. Zhang, X. F. Wang, Z. C. Wang et al., "Current potential therapeutic strategies targeting the TGF-β/Smad signaling pathway to attenuate keloid and hypertrophic scar formation," *Biomedicine & Pharmacotherapy*, vol. 129, Article ID 110287, 2020.

[3] B. E. Cohen, R. G. Geronemus, D. H. McDaniel, and J. A. Brauer, "The role of elastic fibers in scar formation and treatment," *Dermatologic Surgery*, vol. 43, no. 1, pp. S19–S24, 2017.

[4] S. Korntner, C. Lehner, R. Gehwolf et al., "Limiting angiogenesis to modulate scar formation," *Advanced Drug Delivery Reviews*, vol. 146, pp. 170–189, 2019.

[5] Y. Qiao, X. Chang, J. Y. Zheng et al., "Self-interpenetrated water-stable microporous metal-organic framework toward storage and purification of light hydrocarbons," *Inorganic Chemistry*, vol. 60, no. 4, pp. 2749–2755, 2021.

[6] J. X. Li, Z. B. Qin, Y. H. Li, and G. H. Cui, "Visible-light-driven photocatalyst for the degradation of methylene blue over a 3D cobalt(II)-4, 4'-oxybis (benzoate) framework," *Inorganic Chemistry Communications*, vol. 90, pp. 112–114, 2018.

[7] J. C. Yin, Z. Chang, N. Li, J. He, Z. X. Fu, and X. H. Bu, "Efficient regulation of energy transfer in a multicomponent dye-loaded MOF for white-light emission tuning," *ACS Applied Materials & Interfaces*, vol. 12, no. 46, pp. 51589–51597, 2020.

[8] Q. Q. Mu, J. J. Liu, W. B. Chen et al., "A New biscarbazole-based metal-organic framework for efficient host-Guest energy transfer," *Chemistry-A European Journal*, vol. 25, no. 8, pp. 1901–1905, 2019.

[9] G. B. Yang and Z. H. Sun, "Tuning the structural topologies of two luminescent metal-organic frameworks through altering auxiliary ligand," *Inorganic Chemistry Communications*, vol. 29, pp. 94–96, 2013.

[10] M. Du, C. P. Li, C. S. Liu, and S. M. Fang, "Design and construction of coordination polymers with mixed-ligand synthetic strategy," *Coordination Chemistry Reviews*, vol. 257, no. 7-8, pp. 1282–1305, 2013.

[11] Y. H. Tang, X. Wu, F. Wang, and J. Zhang, "Synthesis of zeolite-like metal-organic frameworks via a dual-ligand strategy," *CrystEngComm*, vol. 19, no. 18, pp. 2549–2552, 2017.

[12] C. W. Lv, J. Li, Z. Hou, and M.-k. Li, "Synthesis, structure and luminescent property of a new Zn(II) coordination polymer with isolated tetrahedral {Zn4O} clusters as building subunits," *Inorganic Chemistry Communications*, vol. 36, pp. 1–3, 2013.

[13] Y. P. He, Y. X. Tan, and J. Zhang, "Tuning a layer to a pillared-layer metal–organic framework for adsorption and separation of light hydrocarbons," *Chemical Communications*, vol. 49, no. 96, pp. 11323–11325, 2013.

[14] Y. L. Xu, Q. Gao, M. Zhao, H. J. Zhang, Y. H. Zhang, and Z. Chang, "Impact of the flexibility of pillar linkers on the structure and CO2 adsorption property of pillar-layered MOFs," *Chinese Chemical Letters*, vol. 28, no. 1, pp. 55–59, 2017.

[15] X. Y. Zhao, Y. Li, Z. Chang, L. Chen, and X. H. Bu, "A four-fold interpenetrated metal-organic framework as a fluorescent sensor for volatile organic compounds," *Dalton Transactions*, vol. 45, no. 38, pp. 14888–14892, 2016.

[16] H. Zhu, Y. H. Li, Q. Q. Xiao, and G. H Cui, "Three luminescent Cd(II) coordination polymers containing aromatic dicarboxylate and flexible bis(benzimidazole) ligands as highly sensitive and selective sensors for detection of Cr2O72– oxoanions in water," *Polyhedron*, vol. 187, Article ID 114648, 2020.

[17] H. N. Wang, P. X. Liu, H. Chen, N. Xu, Z. Y. Zhou, and S. P. Zhuo, "Tubular porous coordination polymer for the selective sensing of Cu2+ ions and cyclohexane in mixed suspensions of metal ions via fluorescence quenching," *RSC Advances*, vol. 5, no. 80, pp. 65110–65113, 2015.

[18] Z. Tang, H. Chen, Y. Zhang, B. Zheng, S. Zhang, and P. Cheng, "Functional two-dimensional coordination polymer exhibiting luminescence detection of nitroaromatics," *Crystal Growth & Design*, vol. 19, no. 2, pp. 1172–1182, 2019.

[19] J. Chen, J. Dai, S. H. Wang et al., "A 3D cadmium(II) coordination polymer based on rigid ligand 1-tetrazole-4-imidazole-benzene: solvothermal synthesis, crystal structure and tunable luminescent emissions," *Inorganic Chemistry Communications*, vol. 115, Article ID 107887, 2020.

[20] J. Lu, H. F. Wu, W. F. Wang, J. G. Xu, F. K. Zheng, and G. C. Guo, "Calcium-based efficient cathode-ray scintillating metal-organic frameworks constructed from pi-conjugated luminescent motifs," *Chemical Communications*, vol. 55, no. 92, pp. 13816–13819, 2019.

[21] R. P. Ye, X. Zhang, J. Q. Zhai et al., "N-donor ligands enhancing luminescence properties of seven Zn/Cd(ii) MOFs

based on a large rigid π-conjugated carboxylate ligand," *CrystEngComm*, vol. 17, no. 47, pp. 9155–9166, 2015.

[22] R. P. Ye, X. Zhang, L. Zhang, J. Zhang, and Y. G. Yao, "Solvent and pH driven self-assembly of isomeric or isomorphic complexes: crystal structure and luminescent change upon desolvation," *Crystal Growth & Design*, vol. 16, no. 7, pp. 4012–4020, 2016.

[23] G. M. Sheldrick, "Crystal structure refinement with SHELXL," *Acta Crystallographica Section C: Structural Chemistry*, vol. 71, no. 1, pp. 3–8, 2015.

[24] D. Sun, L. L. Han, S. Yuan, Y. K. Deng, M. Z. Xu, and D. F. Sun, "Four new Cd(II) coordination polymers with mixed multidentate N-donors and biphenyl-based polycarboxylate ligands: syntheses, Structures, and photoluminescent properties," *Crystal Growth & Design*, vol. 13, no. 1, pp. 377–385, 2013.

[25] M. Liberka, J. J. Zakrzewski, M. Heczko, M. Reczynski, S.-i. Ohkoshi, and S. Chorazy, "Solvent- and temperature-driven photoluminescence modulation in porous hofmann-type Sr-II-Re-V metal-organic frameworks," *Inorganic Chemistry*, vol. 60, no. 6, pp. 4093–4107, 2021.

[26] R. P. Ye, L. Lin, and Y. G. Yao, "Structural versatility of four coordination polymers based on 5-(1-oxoisoindolin-2-yl) isophthalic acid: magnetic and luminescent properties," *Inorganica Chimica Acta*, vol. 453, pp. 8–15, 2016.